Journal of Advanced Ceramics
2023, **12**(2): 279–295
https://doi.org/10.26599/JAC.2023.9220682
ISSN 2226-4108
CN 10-1154/TQ

Research Article

Open-cell mullite ceramic foams derived from porous geopolymer precursors with tailored porosity

Jiahuan SHAO[a], Chengying BAI[a,*], Xinyu LI[a,*], Kun YANG[a], Ting ZHENG[a], Yingjie QIAO[a], Lili ZHANG[a], Hongqiang LI[b], Paolo COLOMBO[c,d]

[a]*Key Laboratory of Superlight Materials and Surface Technology*, *Ministry of Education*, *College of Materials Science and Chemical Engineering*, *Harbin Engineering University*, *Harbin 150001*, *China*
[b]*College of Civil Engineering*, *Hunan University*, *Changsha 410082*, *China*
[c]*Department of Industrial Engineering*, *University of Padova*, *via Marzolo*, *Padova 35131*, *Italy*
[d]*Department of Materials Science and Engineering*, *The Pennsylvania State University*, *State College 16802*, *USA*

Received: July 14, 2022; Revised: September 23, 2022; Accepted: October 18, 2022

Abstract: Porous geopolymer precursors were firstly prepared by the direct foaming method using bauxite, fly ash (FA), and metakaolin (MK) as raw materials, and porous mullite ceramics were prepared after ammonium ion exchange and then high-temperature sintering. The effects of chemical foaming agent concentration, ion-exchange time, and sintering temperature on porous geopolymer-derived mullite ceramics were studied, and the optimal preparation parameters were found. Studies have shown that the concentration of blowing agent had great influence on open porosity (q) and porosity and cell size distributions of geopolymer samples, which in turn affected their compressive strength (σ). Duration of the ion exchange had no obvious effect on the sintered samples, and the amount of mullite phase increased with the increase in the sintering temperature. Mullite foams, possessing an open-celled porous structure, closely resembling that of the starting porous geopolymers produced by directly foaming, were obtained by firing at high temperatures. Stable mullite ($3Al_2O_3{\cdot}2SiO_2$) ceramic foams with total porosity (ε) of 83.52 vol%, high open porosity of 83.23 vol%, and compressive strength of 1.72 MPa were produced after sintering at 1400 ℃ for 2 h in air without adding any sintering additives using commercial MK, bauxite, and FA as raw materials.

Keywords: porous mullite ceramic; porosity; porous geopolymer precursor; direct foaming; nanophase strengthening

1 Introduction

Mullite phase ($3Al_2O_3{\cdot}2SiO_2$) is the only stable intermediate phase in a Al_2O_3–SiO_2 system under normal pressure, and it rarely exists in nature [1–4]. Since mullite has excellent creep resistance [3,5], high-temperature stability [2,6], and other excellent properties, it has been used to fabricate advanced structural and functional ceramics, and porous ceramics have also received extensive attention due to the unique properties provided by the presence of porosity [7]. Porous mullite has been used in catalyst carriers [8],

* Corresponding authors.
E-mail: C. Bai, chengyingbai@hrbeu.edu.cn;
X. Li, xinyuli@hrbeu.edu.cn

filters [9], refractory materials [10], and other fields. After a long period of research, some mature preparation methods for the porous ceramics have been established, such as the sacrificial template method [11], pore former method [12,13], foam-gelcasting method [14,15], freeze casting method [16], as well as approaches combining multiple methods [17]; but in terms of its complexity and cost, simple preparation methods and low-cost raw materials are more attractive and promising [18].

Due to their high strength, low thermal conductivity, and low shrinkage after molding [19], geopolymers have received more and more attention in many industrial fields [20], especially in replacing traditional cementitious materials and traditional or advanced ceramics [21]. Porous geopolymers possess the excellent properties of the geopolymers and porous materials, and have become a research hotspot in the field of porous inorganic materials. The main methods for preparing the porous geopolymers are the direct foaming method [22,23], replica method [24], sacrificial template method [25], and additive manufacturing [26], among which the direct foaming method is the most widely used.

On the one hand, the geopolymers, comprising several molecular units, are considered as ceramic-like inorganic polymers [27]. On the other hand, nepheline [28–30], leucite [31–33], and pollucite [34,35] ceramics can be easily obtained from them after high-temperature sintering above 800 ℃. Furthermore, alkaline metal ions can be replaced by other cations (e.g., strontium [36], ammonium [37], and copper [38]). Due to low cost and broad availability of the raw materials including solid waste, easy pore formation, high yield, and low shrinkage of the resulting materials [39,40], the method of converting geopolymers to ceramics has attracted increasing attention, especially for the porous ceramics, such as glass ceramic foams [41], porous $SrAl_2Si_2O_8$ ceramics [36], open-cell leucite ceramics [24], porous h-AlN/SiC-based ceramics [42], porous mullite [21], porous cordierite [43], and monoclinic-celsian ceramics [44].

For the mullite ceramics derived from geopolymer precursors, the low aluminum-to-silicon ratio in the geopolymer cannot enable the formation of the aluminum-rich phase of the mullite, but this can be solved by adding additional aluminum-containing raw materials. Furthermore, an ion-exchange process using a NH_4Cl solution can be carried out to eliminate the alkaline ions from the structure and obtain alkali-free mullite ceramics [21,45]. In our work, porous geopolymer precursors were firstly obtained by the direct foaming method using bauxite, fly ash (FA), and metakaolin (MK) as raw mineral materials (sodium lauroyl sarcosinate (LS-30) as the surfactant and hydrogen peroxide (H_2O_2) as the chemical blowing agent). Here, the FA and MK were used as the main sources of silicon, and the high reactivity of the MK toward geopolymerization provided high green strength before the ion-exchange process. The FA possesses some pozzolanic activity, which can modify the compositions and rheological properties of geopolymer slurries [23] and decrease the cost and earn carbon credits as solid waste [46,47]. Moreover, low-cost bauxite was used to provide an additional source of aluminum. Compared with other aluminum sources (Al_2O_3, $Al(OH)_3$, etc.), the presence of impurities (e.g., MoO_3 and TiO_2) and transition metal ions are beneficial for reducing the sintering temperature of the mullite by forming a solid solution. At the same time, the solid solution would improve some physical properties, including thermal expansion behavior and electrical properties [48].

Using the geopolymers as ceramic precursors is an environmentally-friendly and low-cost new route, especially when solid waste materials are applicated as raw materials. Also, impurity oxides including TiO_2, Fe_2O_3, CaO, and MgO are beneficial for the mullite phase formation at relatively low temperatures. In comparison to the previously published literature, this work enables achieving high volume of interconnected porosity, suitable strength, and better-controlled pore morphology using an environmentally friendly, simple processing method.

2 Experimental procedure

2.1 Raw materials and sample preparation

Bauxite (Hengyuan, China), MK (Chenyi, China), and FA (Jianghan Technology Company, China) were used as the raw materials to prepare the mullite. To introduce the porosity, the H_2O_2 solution with various concentrations (3–9 wt%) (diluted from 30 wt% H_2O_2 solution) and LS-30 (Yousuo, China) was employed as the foaming agent and surfactant, respectively.

According to the chemical formula of the mullite ($3Al_2O_3{\cdot}2SiO_2$) and the chemical compositions of the raw materials, the required amount of the raw materials

was computed to achieve a theoretical oxide molar ratio of Al_2O_3 : SiO_2 = 3 : 2. The mixture formulations and chemical compositions of the main raw materials are provided in Table 1. The alkali activator solution was prepared from 7.78 M (16 g) sodium hydroxide (NaOH) solution by dissolving NaOH powders (Dalu, China) and sodium silicate (water glass) solution of 22 g (Litian, China) with a modulus (*M*) of 3.28. The solid-to-liquid mass ratio in the geopolymer slurry was 5.33.

According to the amount of the raw materials, the mass fractions of the low-content oxides in the geopolymer slurry were 7.33 wt% TiO_2, 4.02 wt% Fe_2O_3, 1.86 wt% CaO, and 0.10 wt% MgO. Besides, the as-received raw materials also contain trace amounts of K_2O, Na_2O, P_2O_5, SO_3, etc. The process for preparing the mullite consisted of the preparation of a porous geopolymer green body by directly foaming, followed by ion exchange and sintering. The procedure for obtaining the porous geopolymer is illustrated in Fig. 1; the geopolymer slurry was prepared by successively adding the bauxite, FA, and MK into the activation solution under mechanical stirring at 500 r/min. The slurry was stirred for 20 min after each mineral was added. After that, LS-30 (2 g) and H_2O_2 (7 g) were added successively, stirring at 1000 r/min for 5 min to obtain the foamed slurry. The above experimental processes were all carried out at room temperature. The foamed slurry was then poured into a plastic mold sealed with a sample bag and cured at 35 ℃ for 24 h (to control the decomposition rate of H_2O_2 to obtain a homogeneous porous microstructure) and at 75 ℃ for the next 24 h in an oven (to increase the strength and complete the geopolymerization reaction).

The samples extracted from a mold were cut into cubes (~25 mm × 25 mm × 25 mm) and washed and dried for the next procedure. The samples were ion exchanged using 0.1 mol/L NH_4Cl solution obtained by dissolving solid NH_4Cl (Guangfu, China) for time ranging from 1 to 4 d. The ion-exchanged step was simply achieved by placing the porous samples in beakers of 500 mL filled with the pre-made NH_4Cl solution at room temperature. Finally, the porous samples with and without (control group) the ion-exchanged step were dried and then subjected to thermal treatment in a resistance furnace (GWL-1700, Juxing Kiln, China). The porous samples were heated at 1 ℃/min to 200 ℃ for 1 h, and then heated up to desired temperatures

Table 1 Mixture formulations and chemical compositions of bauxite, MK, and FA

	Component (g)	Al_2O_3 (wt%)	SiO_2 (wt%)	Fe_2O_3 (wt%)	CaO (wt%)	TiO_2 (wt%)	MgO (wt%)	K_2O (wt%)	Na_2O (wt%)	P_2O_5 (wt%)	SO_3 (wt%)	Others (wt%)
Bauxite	49.85	57.36	10.62	7.13	1.33	15.97	0.00	2.54	0.01	1.68	0.06	3.30
MK	17.92	45.57	48.85	2.32	0.80	1.45	0.22	0.19	0.22	0.07	0.08	0.23
FA	7.68	15.16	48.61	14.18	16.95	1.30	0.95	1.30	0.51	0.04	0.31	0.69

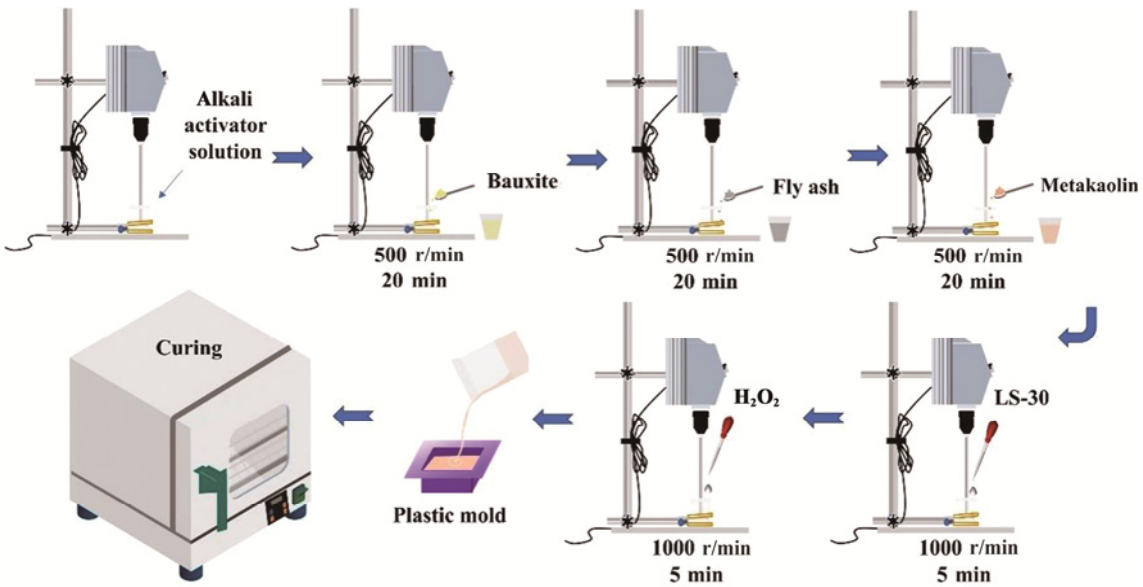

Fig. 1 Schematic illustration of the preparation procedure for porous geopolymer samples.

(1100–1500 ℃) at 5 ℃/min for 2 h, and naturally cooled to room temperature in the furnace.

2.2 Characterization

Compressive strength (σ) was measured using an electronic universal testing machine (WDW-100, Changchun Kexin Test Instrument Co., China) at a rate of 1 mm/min, taking the average value from the testing of four samples.

Surface structures were observed using an optical stereoscopic microscope (BD-61T, Boshida Optical Co., Ltd., China) and a desktop scanning electron microscope (SEM; Phenom pure+, the Netherlands).

X-ray diffraction (XRD) analysis was carried out on powder samples using an X-ray diffractometer (D/MAX-TTRIII, Rigaku Corporation, Japan) with Cu Kα radiation (1.54 Å) at 40 kV and 150 mA, operated with steps of 2θ = 0.02° and a scan rate of 5 s/step.

Open porosity (q, vol%) data were collected using Eq. (1) based on GB/T 25995-2010 [49,50]:

$$q=\frac{100(m_2-m_1)}{m_2-m_3} \tag{1}$$

where m_1 is the dry mass of the sample, m_2 is the mass of the saturated sample in air, and m_3 is the mass of the saturated sample in water.

Also, values of relative density (ρ_r) are analytically calculated based on GB/T 25995-2010 [25,51]:

$$\rho_r=\frac{M_1\rho_l}{M_3-M_2} \tag{2}$$

where ρ_l is the density of the used liquid under the controlled bath constant temperature (water was used in this test, and the density value of water was taken at 25 ℃); M_1 is the amount of the powders in the pycnometer; M_2 is the mass of the sample introduced in the pycnometer filled with water, and M_3 is the mass of only water in the pycnometer.

Values of true density (ρ, g/cm^3) were determined by GB/T 5071-2013 and calculated by Eq. (3):

$$\rho=\frac{M_1\rho_l}{M_3+M_1-M_2} \tag{3}$$

The mean values of ρ of the samples were the average of three measurements. The total porosity (ε, vol%) was calculated by Eq. (4) [51]:

$$\varepsilon = 100(1-\rho_r/\rho) \tag{4}$$

The cell sizes and size distributions were assessed from the SEM images and optical microscope photos using analysis software (Nano Measurer 1.2, Fudan University, China) [52], measuring at least 100 pores/cells per sample. The analysis results were converted to three-dimensional values by Eq. (5) [53]:

$$D_{sphere}=D_{circle}/0.785 \tag{5}$$

where D_{sphere} is the 3D cell size and D_{circle} is the cell size from the software. Thermal gravimetric analysis (TGA) and differential scanning calorimetry (DSC) analysis were analyzed using a TG analyzer (TGA/DSC3+, METTLER TOLEDO, Switzerland) to evaluate thermal decomposition behaviors and phase transformation characteristics of the materials before and after the ion exchange, heating at 10 ℃/min up to 1550 ℃ in air.

Scanning transmission electron microscopy (STEM) images and energy dispersive spectroscopy (EDS) mappings of powder-type specimen (S4) were collected on a transmission electron microscope (Talos F200X, FEI, USA) associated with a dispersive spectrometer (Super-X EDS) with an acceleration voltage of 200 kV. Also, carbon grids of 300 μm were used during the TEM–EDS analyses.

Fourier transform infrared (FTIR) data were collected from the samples mixed with KBr particles using an infrared spectrometer (Nicolet 6700, Thermo Scientific, USA) at wavenumbers of 500–4000 cm^{-1}.

The pH value of the sample was measured using an ion meter (PXSJ-216F, Leici, China) and a pH composite electrode.

Mass change and volume shrinkage of the sample before and after sintering were determined by a precision balance (BSISL, China) and a digital vernier caliper (DEGUQMNI, Germany), respectively.

3 Results and discussion

3.1 Characterization of raw materials

Figures 2(a)–2(c) show the SEM images of the bauxite, FA, and MK. The particle size of the bauxite is between 7 and 40 μm, and that of the FA-contained microsphere is consistent with Ref. [54]. The MK is lamellar, but there are partial agglomerations. Figure 2(d) reports the XRD data for the raw materials. The bauxite contains a large amount of corundum (Al_2O_3; PDF Card No. 00-005-0712), the FA contains silicon oxide (SiO_2; PDF Card Nos. 00-033-1161 and 00-011-0695), and the MK contains quartz (SiO_2; PDF Card No. 97-002-7832) and anatase (TiO_2; PDF Card No.

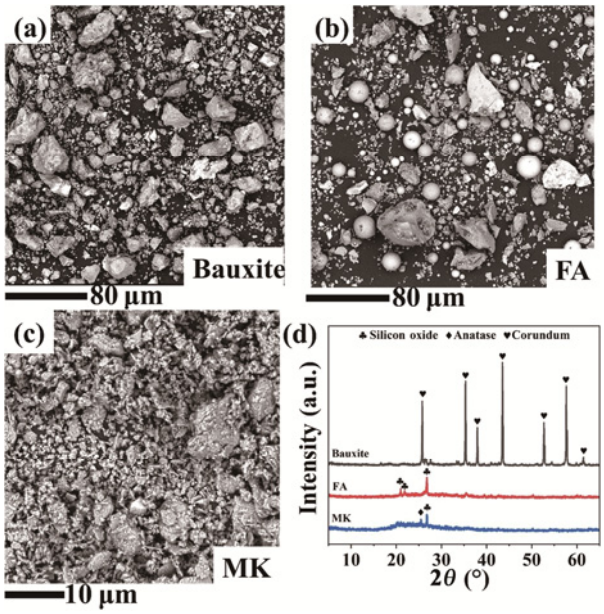

Fig. 2 (a–c) SEM images and (d) XRD patterns of individual raw materials.

97-015-4609) as impurities with a broad amorphous band at 2θ = 15°–35°. The XRD test results of the FA and MK show that both of them contain a (reactive) amorphous phase, and the results correspond to the chemical compositions, as shown in Table 1.

3. 2 Effect of different concentrations of H_2O_2

Gases are generated when the blowing agent is mixed into the geopolymer, creating a network of macropores in the hardened material. Commonly used blowing agents are metal aluminum powders, metal silicon, and H_2O_2; however, metal powders usually produce foams with closed porosity and an inhomogeneous microstructure. H_2O_2 generates gas at the molecular level, and the resulting foam has a more uniform morphology with respect to that obtained by frothing. H_2O_2 is thermodynamically unstable in an alkaline medium and easily decomposes into water and oxygen, and then the bubbles trapped in the paste expand to larger voids [55]. H_2O_2 as a foaming agent for preparing geopolymer foams has the advantage of providing increased strength and a large number of interconnected pores, when a surfactant or stabilizing agent is present [56]. The surfactant was added to achieve foam stabilization by reducing the surface tension of the air–slurry system, Ostwald ripening (bubble coalescence), liquid film rupture, and drainage [57,58]. Taking into account the balance among (total and open) porosity, average cell size, as well as compressive strength, LS-30 was selected among sodium dodecyl sulfate (K12), dodecyl trimethylammonium chloride (liquid 1231), protein sodium cocoyl glycine (AK-301), and lauryl amphoteric diacetate disodium (LAD-40) in this study (Fig. S1 in the Electronic Supplementary Material (ESM)).

The first tests were conducted to explore the effect of different concentrations of H_2O_2 on the geopolymer precursor slurry. The amount of O_2 decomposed from H_2O_2 of different concentrations is also different. In this experiment, 3, 5, 7, and 9 wt% H_2O_2 were added to the slurry, and the addition of the LS-30 surfactant helped retain O_2 in the slurry and stabilize the water–gas interface in the liquid foam. Figure 3 shows the optical and SEM images of the samples with different concentrations of H_2O_2. It can be seen that there are many open cells in the samples, and that the pore distribution was homogeneous in all samples. The number of pores was reduced, but their size increased with the increase in the H_2O_2 concentration, and the cell size could even reach a value of ~3500 μm. This trend is consistent with Refs. [59–62] with different H_2O_2 contents. The average cell diameters were 770.42± 185.23 μm (3 wt% H_2O_2, Fig. 3(a)), 1027.94±280.90 μm (5 wt% H_2O_2, Fig. 3(b)), 1326.01±423.03 μm (7 wt% H_2O_2, Fig. 3(c)), and 1518.09±577.25 μm (9 wt% H_2O_2, Fig. 3(d)).

Figure 4(a) shows the relationship between the open porosity, the total porosity, and the compression strength of the samples with different concentrations of H_2O_2. As the concentration of H_2O_2 increased from 3% to 9%, the open porosity increased from 77.19 to 86.02 vol%, and the total porosity increased from 79.94 to 88.13 vol%, while the compressive strength decreased from 0.80 to 0.11 MPa. These trends are similar to the findings reported by Refs. [59–62] using the FA and MK as the main raw mineral materials and H_2O_2 as a blowing agent. The higher strength is associated with thicker strut dimensions, as shown in Fig. 3.

The relationship between the compressive strength (σ) and total porosity (ε) of the samples can be fitted using the MSA model. Combined with Refs. [25,58] and the pore morphology (Fig. 3), we can assume that the pore shape and average cell size are not the key factors affecting the MSA model. The model can be simplified to $\sigma = \sigma_0 \exp(-b\varepsilon)$, where σ_0 is the theoretical strength when the porosity is 0, and b is the characteristic constant [49,63]. The R^2 (the correlation

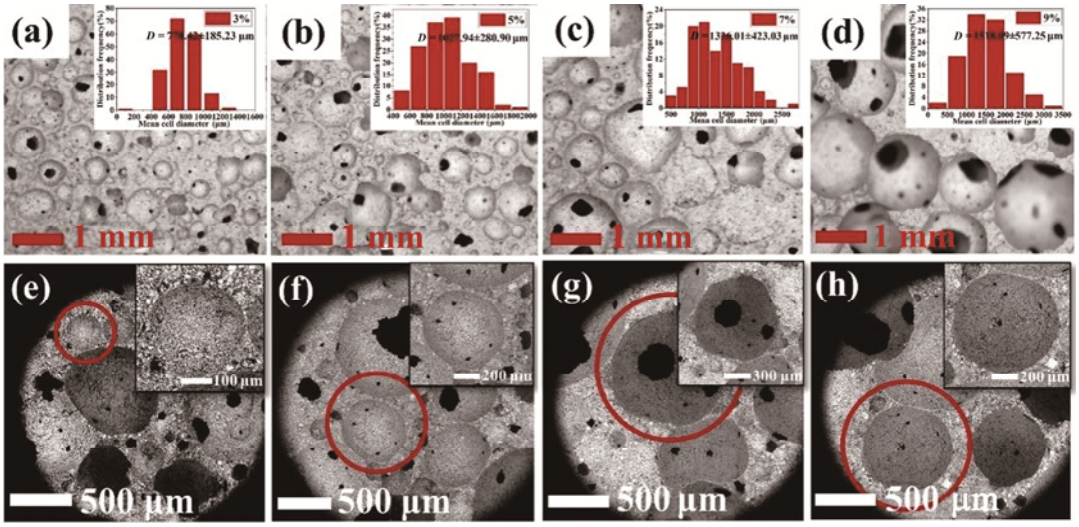

Fig. 3 Optical and SEM images and average cell size distributions of samples with H_2O_2 concentrations of (a, e) 3%, (b, f) 5%, (c, g) 7%, and (d, h) 9%.

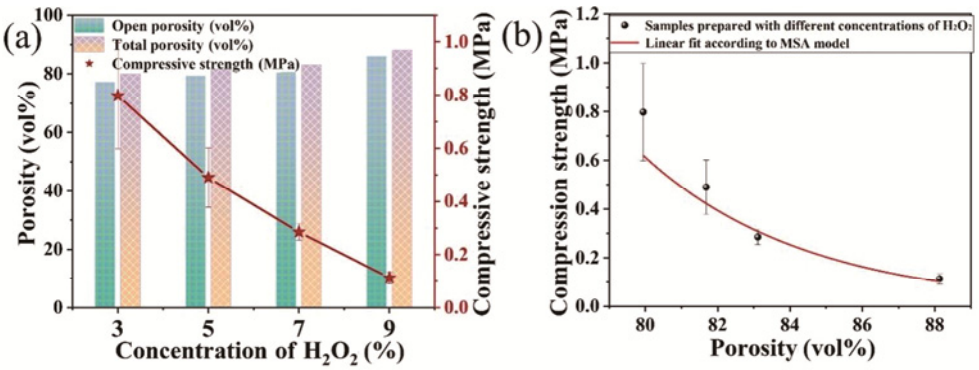

Fig. 4 (a) Compressive strength and porosity vs. concentration of H_2O_2 and (b) porosity and strength of the samples fitted according to the minimum solid area (MSA) model.

factor) obtained after fitting was about 0.95, as shown in Fig. 4(b), indicating that the compressive strength has a high correlation with the porosity as expected.

Figure 5 shows the compressive strength and porosity of the geopolymer samples produced in this work, compared with the previous research data for porous geopolymers obtained using the FA and MK as the raw materials. It can be seen that the porosity of the samples prepared in this study is higher than those of the previous works by directly foaming with various alkaline activators and foaming agents (15M K-based+Tween80/TritonX-100 [64], 10M Na-based+H_2O_2 [60], 8M Na-based+H_2O_2 [61], 12M Na-based+H_2O_2 [62], and Na-based+FA+MK+calcium stearate (CaSt)+Na_2O_2 [23]). The results indicate that the high strength and high porosity can be achieved even after modifying the chemical compositions of the geopolymers obtained by directly foaming, and the produced materials are stable porous precursors for the subsequent ion-exchange and ceramization steps. According to the collected data for the compressive strength and total porosity, the porous

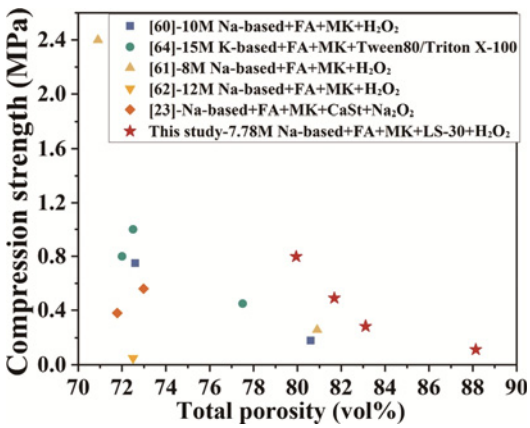

Fig. 5 Comparison of porosity and compressive strength for the samples produced in this work with those for porous geopolymers manufactured using FA and MK as the main raw materials, reported in Refs. [23,60–62,64].

geopolymer precursors with high porosity and competitive strength were obtained by the synergistic action of the foaming agent and surfactant. Also, the samples manufactured using 7% H_2O_2 were selected to investigate the effect of ion-exchange time and the sintering temperature.

3. 3 Effect of ion-exchange time

The alumino–silicate network contains the mobile alkali ions bonded to charge balance sites, which can be replaced by other cations, endowing the material with new functionalities or/and improved properties [21,40]. References [65,66] show that the geopolymer has high affinity for NH_4^+, and the charge balancing Na^+ cations in the geopolymer aluminosilicate network can be exchanged by NH_4^+ with an efficiency close to 100%. After the foam samples with the selected geopolymer formulation were produced, the ion exchange was carried out to obtain alkali-free ceramics by exchanging the alkali ions with ammonium ions. Ion-exchange time of 1, 2, 3, and 4 d was tested.

Figure 6(a) shows the FTIR data of the sample before and after the ion exchange. The sample before and after the ion exchange shows similar wavebands at wavenumbers of 3434–3451 and 1643–1656 cm^{-1}, respectively, which are due to stretching and bending vibrations of water molecules, respectively [67,68]. Energy bands with wavenumbers of 1019–1031 and 599–638 cm^{-1} are attributable to the stretching vibrations of Si–O–Si and Si–O–Al of the geopolymer network, respectively [69]. The bands located at 3232 and 1403 cm^{-1} can be assigned to the vibration of the NH_4^+ group in the sample [70] generated by the ion exchange of NH_4^+ with Na^+ [71]. Meanwhile, the XRD pattern for the geopolymer sample was also collected. While the characteristic "hump" for the geopolymer gel from the XRD data cannot observed (Figs. S2(a) and S2(b) in the ESM) due to the strong peak for Al_2O_3, the typical broad characteristic hump for the MK located in the 2θ range of 2θ = 15°–35° disappeared, providing further evidence for the formation of the geopolymer gel as well [58,65,69]. Figure 6(b) shows the open porosity and total porosity of the samples after sintering for different ion-exchange days. As the number of ion-exchange days increased, the open porosity first increased moderately and then decreased, while the amount of the total porosity remained relatively stable.

The samples after different ion-exchange time were sintered at 1400 ℃ for 2 h, and their properties were tested to determine the optimal number of the ion-exchange days. Surface morphologies of the samples were analyzed using the optical microscope and SEM, and the relationship between force and displacement was assessed, while the cell size distribution analysis was carried out using optical photographs. Since the collected data did not show much difference among the various samples, they were placed in Fig. S3 in the ESM. The reason for this may be linked to the high porosity of the samples, which overrides other contributions, or the fact that the alkali ions could have been completely replaced already within 1–2 d of the ion-exchange treatment.

Since the total porosity and strength values of the samples obtained after 2 d of the ion exchange and sintering were relatively high, the next experiments of investigating the optimal sintering temperature were carried out on this material.

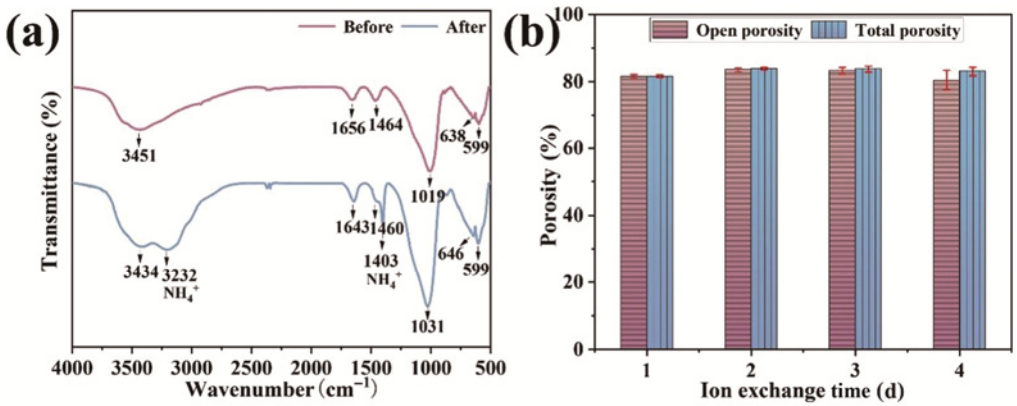

Fig. 6 (a) FTIR spectra of porous geopolymer sample before and after ion exchange and (b) open porosity and total porosity vs. ion-exchange time.

3.4 Effect of sintering temperature

After investigating the concentration of the added H_2O_2 and the number of the ion-exchange days, the optimal sintering temperature was studied as well. The samples after 2 d of the ion exchange were sintered to 1100, 1200, 1300, 1400, and 1500 ℃, labeled as S1, S2, S3, S4, and S5, respectively. For comparison, the samples without the ion exchange were sintered to 1100 and 1200 ℃, denoted as S6 and S7, respectively (Table 2); it should be noted that, it was not possible to use higher sintering temperatures due to the formation of a Na-containing, viscous glass phase, which led to the collapse of the samples during heating (see the second paragraph from bottom).

Figure S4 in the ESM shows the optical images and cell size distributions of the ion-exchanged and non-ion-exchanged samples at different sintering temperatures. The data indicate that the cell size distributions of the ion-exchanged sample did not change much with the sintering temperature, but that of the non-ion-exchanged sample had a more inhomogeneous pore structure; more significantly, it also exhibited the presence of a glassy phase, suggesting that some viscous deformation occurred during sintering.

Figure 7 shows the change in the microstructure with the sintering temperature ranging from 1100 to 1500 ℃. It can be observed that with the increase in the sintering temperature, the microstructure of the sample also changed significantly. A needle-like crystal structure appeared (the inset of Fig. 7(c)) when the sintering temperature reached 1300 ℃, and the elongated needle-like crystals were inferred as a mullite phase considering that a needle-like shape is the representative crystal structure of the mullite [72–74], which was further confirmed by the subsequent XRD data (Fig. 9). When the sintering temperature was 1400 ℃, the bauxite reacted with the silicon-containing phases, and the rectangular secondary mullite formed from a transient liquid phase through dissolution–precipitation mechanism (compared later in Fig. 9). The thicker and longer mullite crystals were interlocked with each other [9,75,76]. Due to sintering densification, the enlarged mullite crystals sintered together, and the total porosity slightly dropped for the porous ceramics after higher sintering temperature (1500 ℃) (Table 2). The results for the optical (Fig. S4 in the ESM) and SEM images (Fig. 7) of the obtained porous ceramics together with those of the porous geopolymer precursors (Fig. 3) showed that the morphology of the porous geopolymer precursors was well retained by the mullite foams after sintering, even with a large volume shrinkage (18.11%–27.46%). A small amount of the glassy phase was observed up to the sintering temperature of 1500 ℃ (S5), and the total porosity and open porosity were still quite high (81.43 and 80.93 vol%, respectively).

Figure 8 shows the TGA–DSC curves of the geopolymer precursor samples with and without the ion exchange. The thermal decomposition and phase change processes of the samples during combustion in air were studied. For both samples, two exothermic peaks were present at approximately 258 ℃. The first mass loss in 25–200 ℃ corresponds to the first obvious exothermic peak, which is due to the decomposition of organic matter in the raw materials [10,56,77], and the second mass loss is due to the decomposition and combustion of the surfactant [41,78], which corresponds to the second exothermic peak with a peak value around 325 ℃ [79]. A peak corresponding to the NH_4^+ decomposition was not found in the DSC pattern,

Table 2 ρ_r, **open porosity, total porosity, compression strength, volume shrinkage, and weigh loss data of different samples after sintering**

Sample	Sintering temperature (℃)	ρ_r (g/cm^3)	Open porosity (vol%)	Total porosity (vol%)	Compression strength (MPa)	Volume shrinkage (%)	Weight loss (%)
S1	1100	0.50±0.01	83.62±0.30	84.20±0.26	0.58±0.20	18.11±0.76	7.68±0.12
S2	1200	0.52±0.01	83.04±0.36	83.29±0.30	1.34±0.49	22.12±0.13	7.73±0.13
S3	1300	0.52±0.01	83.00±0.46	83.48±0.28	1.68±0.60	22.25±0.19	7.56±0.17
S4	1400	0.51±0.02	83.23±0.94	83.52±0.78	1.72±0.79	19.51±1.02	7.56±0.15
S5	1500	0.59±0.03	80.93±0.71	81.43±0.80	2.31±0.23	27.46±1.24	7.80±0.09
S6	1100	0.58±0.03	80.46±1.02	81.37±1.03	1.41±0.67	23.26±0.74	8.28±0.63
S7	1200	0.93±0.05	68.19±2.20	n.d.	n.d.	~55.01±3.13	8.12±0.25

Note: n.d. represents “not determined due to melting”.

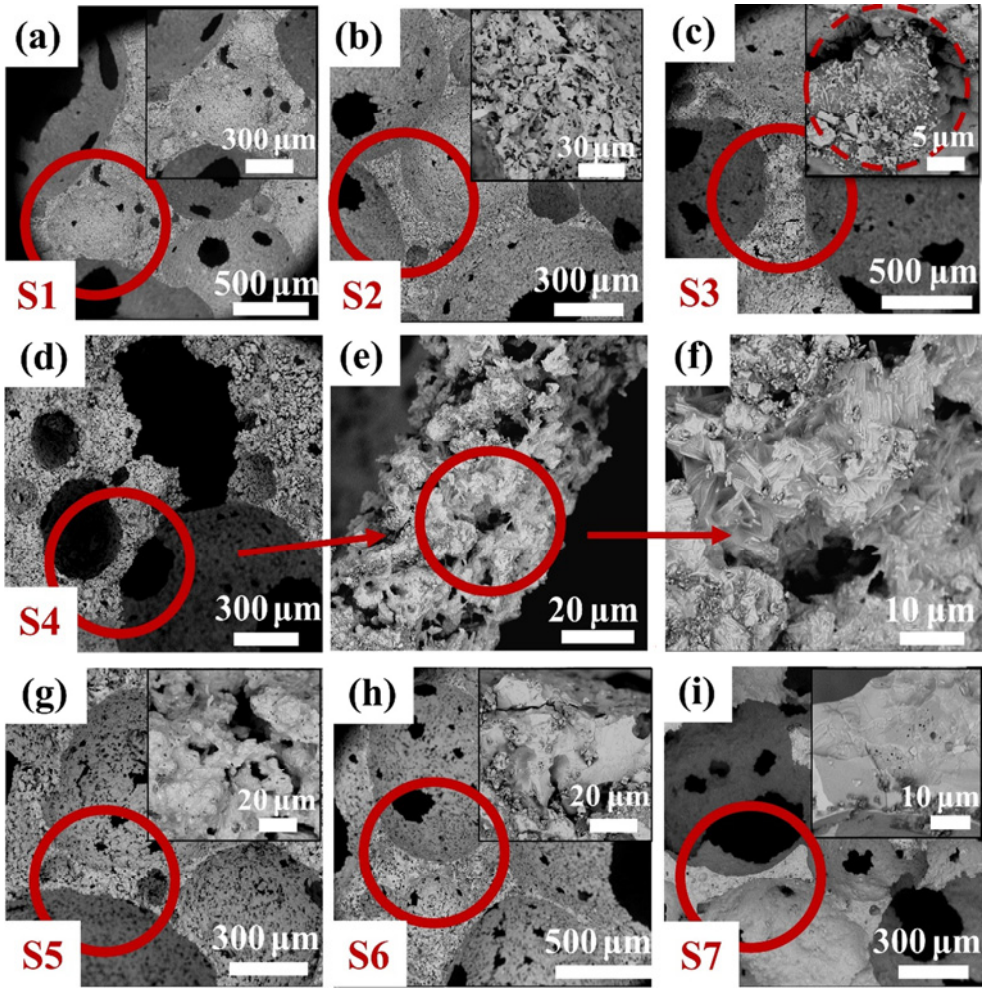

Fig. 7 SEM images for porous samples at various sintering temperatures: (a) S1 (1100 ℃), (b) S2 (1200 ℃), (c) S3 (1300 ℃), (d–f) S4 (1400 ℃), (g) S5 (1500 ℃), (h) S6 (1100 ℃), and (i) S7 (1200 ℃).

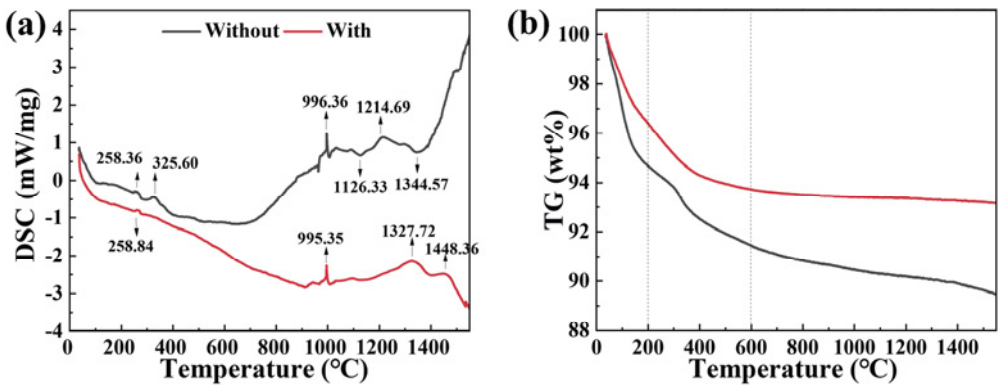

Fig. 8 (a) DSC and (b) TGA curves of the samples with and without ion exchange, analyzed at a heating rate of 10 ℃/min in air.

possibly due to the fact that the exothermic peak produced by the NH_4^+ decomposition and the endothermic peak of dehydration occur simultaneously at about 100 ℃, overlapping and making it hard to observe [80]. It is interesting to observe two sharp exothermic peaks at about 995 ℃. The exothermic peak for the sample without the ion exchange at ~996 ℃ was probably associated with the crystallization

of the sodium alumino–silicate phase (nepheline) or to the Al–Si spinel and amorphous silica [81–83], and the exothermic peak for the sample with the ion exchange at ~995 ℃ could be ascribed to the formation of the mullite [84,85] or to the Al–Si spinel [82,83,86]. It should be noted that the peaks in the DSC curve were affected by the composition [87] and heating rate [83,88]. More accurate investigations on the phase evolution occurring within this temperature range will have to be carried out by carefully heat-treating the samples at smaller temperature intervals. The sample after the ion exchange had two obvious exothermic peaks between 1300 and 1500 ℃, but there was no significant weight loss. It can be inferred that the corundum and the cristobalite reacted to form the mullite [89].

According to the TGA curve, the weight loss of the sample after the ion exchange was 6.85% after sintering, while that of the control sample without the ion exchange was 10.50%. The higher weight loss trend at temperatures less than 600 ℃ can be explained considering the content of the surfactant, as the water-soluble impurities and surfactant were also removed after the ion-exchange treatment, which can be confirmed by the vanishing exothermic peak (325 ℃) in the DSC data. A continuous weight loss trend was observed for the control sample without the ion-exchange treatment above 600 ℃. The weight loss phenomenon could be explained by the volatilization of low-melting-point metal oxides [90–93] and their compounds [93–95] at high temperatures. This loss was also detected for the starting materials (bauxite [96] and FA [13]), and the porous structure for the samples without the ion exchange sintered at 1300 ℃ could not be maintained due to the formation of a glass phase (vitrification). Moreover, two endothermic peaks at 1126.33 and 1344.57 ℃ were detected, which could be attributed to glass melting. To verify the consistency of the TGA data, the actual weight loss of the samples after sintering was also accorded (Table 2).

As shown in Fig. 9, the ion exchange had a great influence on the phase assemblage development. The samples without the ion exchange formed a glass-based composite material after sintering, with the main crystalline phase of Al_2O_3 (S6: PDF Card No. 97-007-3724 and S7: PDF Card No. 97-007-7810). Also, small amounts of nepheline phase (S6: PDF Card No. 00-035-0424) and albite phase (S7: PDF Card No. 00-010-0393) were also detected [97]. After the ion exchange, a reaction occurred, and the mullite (S2–S5: PDF Card No. 00-015-0776) appeared. Starting from the sintering temperature of 1200 ℃, the amount of the mullite phase gradually increased from 29.9 to 99.1 wt% according to Rietveld peak refinement (Fig. S5 in the ESM), while the peak intensities of the corundum (S1 and S3: PDF Card No. 97-007-3724, S2: PDF Card No. 97-003-1545, S4: PDF Card No. 97-007-3076, and S5: PDF Card No. 97-016-5594) and cristobalite phases (S1 and S2: PDF Card No. 97-007-4530) gradually decreased, with the cristobalite disappearing in the end when heating above 1300 ℃, especially at 1500 ℃ due to the thermal-induced crystallization. Therefore, we can infer that the mullite formed because of the solid-state reaction among the corundum, cristobalite, and geopolymer phases, which is also confirmed by the endothermic peaks at 1327.72 and 1448.36 ℃ in the DSC curve (Fig. 8(a)). After 1400 ℃, the amount of the mullite crystals hardly changed with the sintering temperature, mullitization being almost complete before 1500 ℃. Reference [98] shows that the raw materials have a great influence on the reaction in the Al_2O_3–SiO_2 system, with SiO_2 and Al_2O_3 producing the mullite at around 1400 ℃ through the solution precipitation mechanism, with the formation of the mullite being controlled by diffusion, consistent with the present study. Furthermore, the raw materials in the bauxite, MK, and FA contain a small amount of impurities (TiO_2, Fe_2O_3, CaO, and MgO), which can react with SiO_2 and Al_2O_3 before reaching the melting temperature, forming a liquid at high sintering temperatures and promoting the growth of mullite crystals. Reference [99] shows that TiO_2 and Fe_2O_3 react with Al_2O_3 and SiO_2 to form low-melting silicate minerals, and a large amount of the liquid phase is formed during sintering. This liquid phase is conducive to the formation of secondary mullite and also has a positive effect on the sintering of the mullite. Moreover, the presence of Fe_2O_3, MgO, and CaO promotes the growth of the mullite crystals by reducing the liquid viscosity [100]. It should be noted that Ca^{2+} and Mg^{2+} ions can be replaced by the NH_4^+ ions in the process of the ion exchange as well [45,101]. In any case, the content of CaO and MgO is low, and therefore the lower sintering temperature for the mullite phase can be mainly attributed to the TiO_2 and Fe_2O_3 impurities in this study.

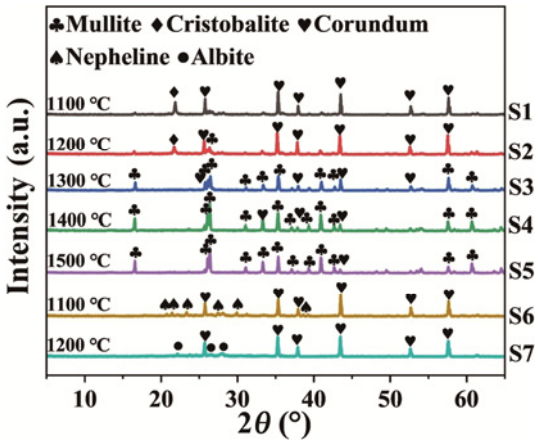

Fig. 9 XRD patterns of ion-exchanged (S1–S5) and non-ion-exchanged (S6 and S7) samples at different sintering temperatures.

Figures 10(a)–10(d) report bright-field TEM images and the corresponding selected area electron diffraction (SAED) patterns of the circled area for the sample S4 (sintered at 1400℃). Rod-shaped crystals with a length of around 700 nm coexisted with numerous nanocrystals with grain sizes of around 30 nm, as shown in the bright-field TEM image and further evidenced by the poly-crystalline rings in the SAED patterns. The nanoclusters coexisting with the mullite poly-crystalline phases can strengthen the material by hindering the cracking propagation by enhancing the grain boundary density, as shown in Fig. 10. Similar phenomena have widely been reported for various ceramic systems including pyrochlore and fluorite [102]. The bright spots can be further indexed as the mullite (PDF Card No. 00-015-0776) on the zone axis [001]. Figures 10(c) and 10(d) show another mullite crystal without a rod shape that grew in the $[\bar{2}\,\bar{1}\,4]$ direction. Figures 10(e)–10(g) report the high-resolution STEM image of the as-sintered mullite nanocrystals and the corresponding fast Fourier transform (FFT) images. The high-resolution TEM images were further validated by the XRD detection results [103,104]. The clear lattice fringes confirmed good crystallinity. The high-resolution STEM images of different regions show that the sample contained little amount of nano-crystalline mullite with a *d* spacing of 0.4 nm and sillimanite ($Al_2O_3 \cdot SiO_2$) with a *d* spacing of 0.37 nm. The presence of the sillimanite with a crystal size of around 10 nm can be attributed to the non-chemical stoichiometric sample preparation or intermediate state of sintering [105–107], which further indicates the complexity of the mullitization behavior. However, the amount of the sillimanite phase is too small to be detected by the XRD. Figure 10(j) reports the measured EDS profile of the mullite; it shows the presence and contents of Si, O, Al, Fe, and Ti elements [108,109], which is consistent with the chemical composition of the raw materials. It should be noted that no Na was found in the sample, indicating that the

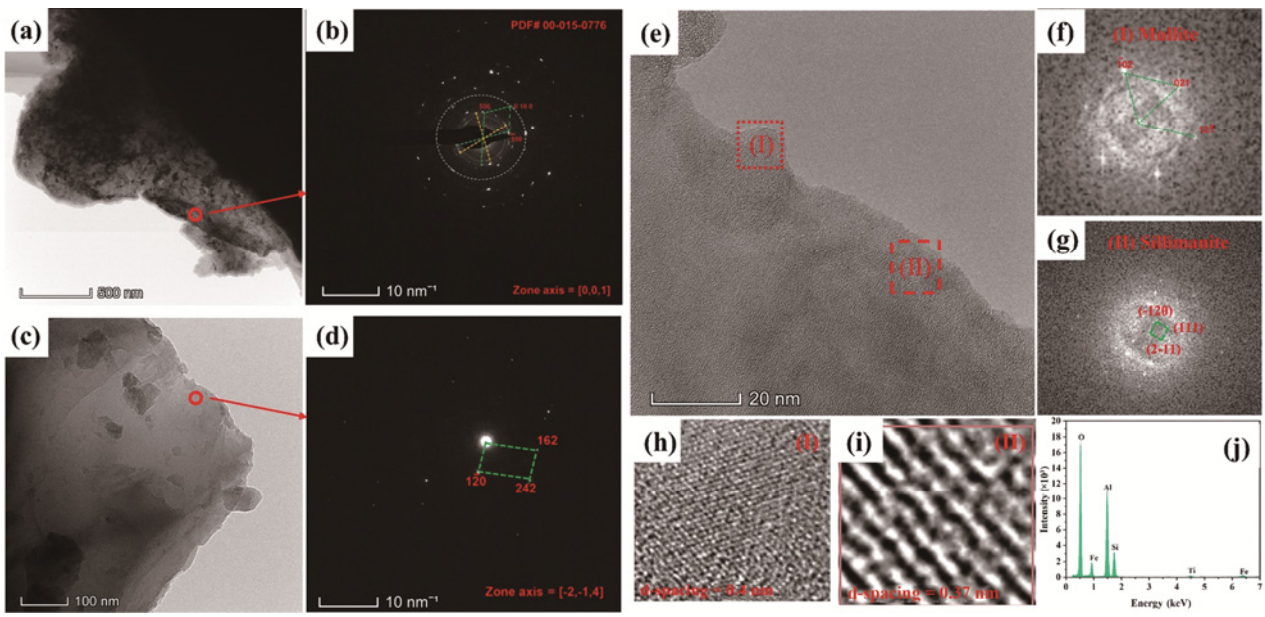

Fig. 10 TEM analyses of the sample S4 sintered at 1400 ℃: (a–d) TEM images and SAED patterns of circled area, (e) high-resolution TEM image, (f, g) FFT analyses of areas (I) and (II) in (e), respectively, (h, i) enlarged images of areas (I) and (II) in (e), respectively, and (j) EDS spectra for individual elements.

ion-exchange process was successful. The Ca and Mg elements were not detected in the EDS data as well, which can be explained by their low contents in the samples; additionally, Ca^{2+} and Mg^{2+} can also be replaced by the NH_4^+ in the process of the ion exchange [45,101].

Table 2 reports the porosity (total porosity and open porosity), ρ_r, compression strength, volume shrinkage, and weight loss data of different samples. As can be seen, the sintering temperature had some influence on the porosity, compressive strength, volume shrinkage, as well as weight loss. As the sintering temperature for the ion-exchanged samples increased, the total porosity decreased from 84.2 to 81.4 vol%, and the compressive strength increased sharply from 0.58 to 2.31 MPa. The weight loss trend of the sample data after sintering is consistent with the TGA curve, and a higher mass loss was observed due to the long dwelling stage (2 h). There was no obvious variation (~20 vol%) for the volume shrinkage when the sintering temperature was lower than 1500 ℃. While the volume shrinkage of the sample sintered at 1500 ℃ reached 27.46% due to the liquid phase densification of the secondary mullite [110], compared with other samples sintered after the ion exchange, the sample sintered at 1400 ℃ had the best compromise among porosity, compressive strength, and volume shrinkage values. The samples without the ion exchange have lower porosity and larger volume shrinkages, certainly due to the formation of a viscous, Na-containing glass phase during sintering, which led to the partial collapse of the structure after firing at 1200 ℃.

The porosity and mechanical characteristics of the mullite prepared using various pore-forming methods and sintered at about 1400 ℃ are compared in Table 3. We can observe that within the sintering temperature range of 1350–1450 ℃, the compressive strength for

Table 3 Raw materials, fabrication methods and processing conditions, total porosity, open porosity, compressive strength, and mean cell diameters of porous mullite ceramics produced using different raw materials and processing approaches

Main raw materials	Fabrication method	Processing condition	Total porosity (%)	Open porosity (%)	Compressive strength (MPa)	Mean cell diameter (μm)	Ref.
Mullite whiskers, $CaCO_3$, α-Al_2O_3, and SiO_2	Seed-assisted *in situ* synthesis and foam-freeze casting techniques	1350 ℃, 5 h	—	87.7–90.2	0.65–3.31	—	[104]
Mullite fibers, polyethyleneimine, SiC, starch, and B_4C	Vacuum squeeze molding	1400 ℃, 1 h	79.4–87.3	—	0.81–2.46	—	[111]
Polycrystalline mullite fibers, silica sol, and starch	Pore former method	1400 ℃, 1 h	—	76.4	1.86	—	[112]
Calcined clay, kaolin clay, kyanite, and precipitated calcium carbonate	Foam-gelcasting method	1350 ℃, 3 h	—	77.9	2.49	100–500	[113]
Mullite and $ZrSiO_4$	Foam-gelcasting method	1400 ℃, 2 h	77–78	—	3.93–9.54	141.9–171	[114]
Polycrystalline mullite fibers, alumina, and SiC powders	Gel-casting	1400 ℃, 4 h	—	71.7	4.4	~5	[115]
FA and calcined bauxite	Particle stabilization method	1400 ℃, 2 h	72.3	—	31	—	[116]
Mullite powders	Foam-gelcasting method	1350 ℃	—	81.6	3	—	[117]
Fused mullite powders	Foam-gelcasting method	1400 ℃, 5 h	—	81.2	4	—	[118]
Kyanite powders and Al_2O_3	Foaming method	1450 ℃, 3 h	77.3	—	5.5	2.5–9.1	[119]
Fused mullite powders	Foaming and starch consolidation method	1400 ℃, 2 h	85	—	2.4	—	[120]
Polycrystalline mullite fiber, zirconia fiber, SiC, starch, B_4C, and Al_2O_3–SiO_2 sols	Vacuum squeeze molding and sol–gel impregnation	1400 ℃, 1 h	—	87.4–89.8	0.91–1.36	—	[121]
Mullite, kaolin, and aluminum dihydrogen phosphate	Polymeric sponge replication method	1400 ℃, 4 h	—	86.8	1.32	—	[122]
Alumina and silicon dioxide	Organic foam impregnation method	1400 ℃, 2 h	—	87.8	3.1	—	[123]
Fused mullite powders	Foaming and starch consolidation method	1400 ℃	84.8	—	1.52	—	[124]
Bauxite, MK, and FA	Direct foaming method + geopolymer precursor	1400 ℃, 2 h	83.52	83.23	1.72	1320.04	This work

the mullite ceramics (S4) obtained in this work was similar or even higher than those of other mullite foams at similar porosity levels [111–119], although higher strength than the one for the sample S4, even associated with higher porosity, can be also achieved [104,120–124]. However, we can state that these mullite foams obtained from the porous geopolymers possessing high mechanical strength, high open porosity, and homogeneous microstructures are competitive at similar porosity levels and sintering temperatures because of using lower-cost raw materials [112,121], being manufactured using easier foaming steps [104, 111,121] and not requiring additional sintering aids (SiC and B_4C) [111,115,121] nor various types of mullite seeds (fiber [111,112,115,121], whisker [104], and powders [114,117,118,120,122,124]).

4 Conclusions

An effective method for the preparation of low-cost, high-porosity, large-cell-size, and high-connectivity porous mullite ceramics using porous geopolymer precursors at low temperatures without adding sintering additives was proposed. The effect of the chemical foaming agent concentration and ion-exchange time on the porosity, cellular morphology, and mechanical properties of the porous geopolymer precursors was investigated. Also, the influence of the sintering temperature on the final mullite ceramics was studied.

The main points can be described as follows:

(1) Open-cell geopolymer foam precursors with designed $3Al_2O_3/2SiO_2$ compositions and acceptable compressive strength were fabricated by directly foaming using LS-30 as the stabilizing agent, and the porosity can be easily tailored by the content of the chemical pore-forming agent (H_2O_2). The relation between the total porosity and the compressive strength can be well explained by the MSA model.

(2) The Na^+ ions can be replaced by the NH_4^+ ions via a simple ion-exchange route, while the ion-exchange time (1–4 d) had a weak effect on the porosity and mechanical performance. After the ion exchange and sintering (1100–1500 ℃), the porous mullite ceramics were obtained using the porous geopolymers as precursors. Commercial raw materials (MK, bauxite, and FA) contain a small amount of oxide impurities including TiO_2 and Fe_2O_3, which can generate a liquid phase, promoting the growth of the mullite and reducing the sintering temperature of the mullite.

(3) The prepared open-cell mullite foams, with tailored porosity as well as the advantage of using a sustainable and low-cost manufacturing process, can be used as high-temperature filters, refractory materials, membrane supports, and porous scaffolds.

Acknowledgements

This work was supported by the National Natural Science Foundation of China (52002090), the Heilongjiang Postdoctoral Science Foundation Funded Project (LBH-Z19051), the Fundamental Research Funds for the Central Universities (XK21000210), the Scientific Research Foundation for the Returned Overseas Chinese Scholars of Heilongjiang Province (2019QD0002), and the open fund from Key Laboratory of Superlight Materials and Surface Technology, Ministry of Education (XK2100021044).

Declaration of competing interest

The authors have no competing interests to declare that are relevant to the content of this article.

Electronic Supplementary Material

Supplementary material is available in the online version of this article at https://doi.org/10.26599/JAC.2023.9220682.

References

[1] Sanya OT, Owoeye SS, Isinkaye OE, *et al*. Chemical, phase and structural change of mullite synthesized during sintering of kaolin. *Int J Appl Ceram Technol* 2020, **17**: 2259–2264.

[2] Duval DJ, Risbud SH, Shackelford JF. Mullite. In: *Ceramic and Glass Materials: Structure, Properties and Processing*. Shackelford JF, Doremus RH, Eds. New York: Springer New York, 2008: 27–39.

[3] Ashwell J. Mullite for structural, electronic, and optical applications. *Phys Chem Chem Phys* 2003, **74**: 1991–2003.

[4] Schneider H, Schreuer J, Hildmann B. Structure and properties of mullite—A review. *J Eur Ceram Soc* 2008, **28**: 329–344.

[5] Torrecillas R, Calderón JM, Moya JS, *et al*. Suitability of mullite for high temperature applications. *J Eur Ceram Soc* 1999, **19**: 2519–2527.

[6] Roy R, Das D, Rout PK. A review of advanced mullite ceramics. *Eng Sci* 2022, **18**: 20–30.

[7] He ZY. Fabrication and microstructures improvement of porous mullite ceramics based on sol-treated sawdust. *J Ceram Soc Jpn* 2020, **128**: 254–259.
[8] Buciuman FC, Kraushaar-Czarnetzki B. Ceramic foam monoliths as catalyst carriers. 1. Adjustment and description of the morphology. *Ind Eng Chem Res* 2003, **42**: 1863–1869.
[9] Zhu ZW, Wei ZL, Sun WP, *et al*. Cost-effective utilization of mineral-based raw materials for preparation of porous mullite ceramic membranes via *in situ* reaction method. *Appl Clay Sci* 2016, **120**: 135–141.
[10] Ge ST, Lin LX, Zhang HJ, *et al*. Synthesis of hierarchically porous mullite ceramics with improved thermal insulation via foam-gelcasting combined with pore former addition. *Adv Appl Ceram* 2018, **117**: 493–499.
[11] Kim YW, Kim HD, Park CB. Processing of microcellular mullite. *J Am Ceram Soc* 2005, **88**: 3311–3315.
[12] Chen S, Cai WH, Wu JM, *et al*. Porous mullite ceramics with a fully closed-cell structure fabricated by direct coagulation casting using fly ash hollow spheres/kaolin suspension. *Ceram Int* 2020, **46**: 17508–17513.
[13] Qian HR, Cheng XD, Zhang HP, *et al*. Preparation of porous mullite ceramics using fly ash cenosphere as a pore-forming agent by gelcasting process. *Int J Appl Ceram Technol* 2014, **11**: 858–863.
[14] Deng XG, Wang JK, Liu JH, *et al*. Preparation and characterization of porous mullite ceramics via foam-gelcasting. *Ceram Int* 2015, **41**: 9009–9017.
[15] Deng XG, Ran SL, Han L, *et al*. Foam-gelcasting preparation of high-strength self-reinforced porous mullite ceramics. *J Eur Ceram Soc* 2017, **37**: 4059–4066.
[16] Wang Z, Feng PZ, Wang XH, *et al*. Fabrication and properties of freeze-cast mullite foams derived from coal-series kaolin. *Ceram Int* 2016, **42**: 12414–12421.
[17] Liu H, Liu JY, Hong Z, *et al*. Preparation of hollow fiber membranes from mullite particles with aid of sintering additives. *J Adv Ceram* 2021, **10**: 78–87.
[18] Xu XH, Liu X, Wu JF, *et al*. Fabrication and characterization of porous mullite ceramics with ultra-low shrinkage and high porosity via sol–gel and solid state reaction methods. *Ceram Int* 2021, **47**: 20141–20150.
[19] Novais RM, Pullar RC, Labrincha JA. Geopolymer foams: An overview of recent advancements. *Prog Mater Sci* 2020, **109**: 100621.
[20] Bai CY, Colombo P. Processing, properties and applications of highly porous geopolymers: A review. *Ceram Int* 2018, **44**: 16103–16118.
[21] Rincón Romero A, Elsayed H, Bernardo E. Highly porous mullite ceramics from engineered alkali activated suspensions. *J Am Ceram Soc* 2018, **101**: 1036–1041.
[22] Reeb C, Pierlot C, Davy C, *et al*. Incorporation of organic liquids into geopolymer materials—A review of processing, properties and applications. *Ceram Int* 2021, **47**: 7369–7385.
[23] Peng X, Shuai Q, Li H, *et al*. Fabrication and fireproofing performance of the coal fly ash-metakaolin-based geopolymer foams. *Materials* 2020, **13**: 1750.
[24] Kovářík T, Hájek J, Pola M, *et al*. Cellular ceramic foam derived from potassium-based geopolymer composite: Thermal, mechanical and structural properties. *Mater Design* 2021, **198**: 109355.
[25] Wang XD, Li XY, Bai CY, *et al*. Facile synthesis of porous geopolymers via the addition of a water-soluble pore forming agent. *Ceram Int* 2022, **48**: 2853–2864.
[26] Ma SQ, Fu S, Zhao SJ, *et al*. Direct ink writing of geopolymer with high spatial resolution and tunable mechanical properties. *Addit Manuf* 2021, **46**: 102202.
[27] Davidovits J. Geopolymers: Ceramic-like inorganic polymers. *J Ceram Sci Technol* 2017, **8**: 335–350.
[28] Kuenzel C, Grover LM, Vandeperre L, *et al*. Production of nepheline/quartz ceramics from geopolymer mortars. *J Eur Ceram Soc* 2013, **33**: 251–258.
[29] Ahmad R, Abdullah MMAB, Ibrahim WMW, *et al*. Role of sintering temperature in production of nepheline ceramics-based geopolymer with addition of ultra-high molecular weight polyethylene. *Materials* 2021, **14**: 1077.
[30] Liew YM, Heah CY, Li LY, *et al*. Formation of one-part-mixing geopolymers and geopolymer ceramics from geopolymer powder. *Constr Build Mater* 2017, **156**: 9–18.
[31] He PG, Jia DC, Wang SJ. Microstructure and integrity of leucite ceramic derived from potassium-based geopolymer precursor. *J Eur Ceram Soc* 2013, **33**: 689–698.
[32] He PG, Jia DC, Wang MR, *et al*. Thermal evolution and crystallization kinetics of potassium-based geopolymer. *Ceram Int* 2011, **37**: 59–63.
[33] Lin TS, Jia DC, He PG, *et al*. Thermo-mechanical and microstructural characterization of geopolymers with α-Al_2O_3 particle filler. *Int J Thermophys* 2009, **30**: 1568–1577.
[34] He PG, Jia DC. Low-temperature sintered pollucite ceramic from geopolymer precursor using synthetic metakaolin. *J Mater Sci* 2013, **48**: 1812–1818.
[35] He PG, Wang RF, Fu S, *et al*. Safe trapping of cesium into doping-enhanced pollucite structure by geopolymer precursor technique. *J Hazard Mater* 2019, **367**: 577–588.
[36] Zhao SJ, Qin SH, Jia ZL, *et al*. From bulk to porous structures: Tailoring monoclinic $SrAl_2Si_2O_8$ ceramic by geopolymer precursor technique. *J Am Ceram Soc* 2020, **103**: 4957–4968.
[37] O'Leary BG, MacKenzie KJD. Inorganic polymers (geopolymers) as precursors for carbothermal reduction and nitridation (CRN) synthesis of SiAlON ceramics. *J Eur Ceram Soc* 2015, **35**: 2755–2764.
[38] Luukkonen T, Yliniemi J, Sreenivasan H, *et al*. Ag- or Cu-modified geopolymer filters for water treatment manufactured by 3D printing, direct foaming, or granulation. *Sci Rep* 2020, **10**: 7233.
[39] Yu ZJ, Lv X, Mao KW, *et al*. Role of *in-situ* formed free carbon on electromagnetic absorption properties of polymer-derived SiC ceramics. *J Adv Ceram* 2020, **9**: 617–628.

[40] Zhang XH, Bai CY, Qiao YJ, *et al*. Porous geopolymer composites: A review. *Compos Part A-Appl S* 2021, **150**: 106629.
[41] Bai CY, Li HQ, Bernardo E, *et al*. Waste-to-resource preparation of glass-containing foams from geopolymers. *Ceram Int* 2019, **45**: 7196–7202.
[42] Jia DC, Li YH, He PG, *et al*. *In-situ* formation of bulk and porous h-AlN/SiC-based ceramics from geopolymer technique. *Ceram Int* 2019, **45**: 24727–24733.
[43] Romero AR, Elsayed H, Bernardo E. Highly porous cordierite ceramics from engineered basic activation of metakaolin/talc aqueous suspensions. *J Eur Ceram Soc* 2020, **40**: 6254–6258.
[44] Fu S, He PG, Wang MR, *et al*. Monoclinic-celsian ceramics formation: Through thermal treatment of ion-exchanged 3D printing geopolymer precursor. *J Eur Ceram Soc* 2019, **39**: 563–573.
[45] O'Connor SJ, MacKenzie KJD, Smith ME, *et al*. Ion exchange in the charge-balancing sites of aluminosilicate inorganic polymers. *J Mater Chem* 2010, **20**: 10234–10240.
[46] Wang C, Xu GG, Gu XY, *et al*. High value-added applications of coal fly ash in the form of porous materials: A review. *Ceram Int* 2021, **47**: 22302–22315.
[47] Li XY, Bai CY, Qiao YJ, *et al*. Preparation, properties and applications of fly ash-based porous geopolymers: A review. *J Clean Prod* 2022, **359**: 132043.
[48] Maldhure AV, Tripathi HS, Ghosh A, *et al*. Mullite–corundum composites from bauxite: Effect of chemical composition. *T Indian Ceram Soc* 2014, **73**: 31–36.
[49] Rice RW. Evaluating porosity parameters for porosity–property relations. *J Am Ceram Soc* 1993, **76**: 1801–1808.
[50] Qiu BF, Duan XM, Zhang Z, *et al*. Microstructural evolution of h-BN matrix composite ceramics with La–Al–Si–O glass phase during hot-pressed sintering. *J Adv Ceram* 2021, **10**: 493–501.
[51] Wang LY, An LQ, Zhao J, *et al*. High-strength porous alumina ceramics prepared from stable wet foams. *J Adv Ceram* 2021, **10**: 852–859.
[52] Li W, Hao JG, Li W, *et al*. Electrical properties and luminescence properties of $0.96(K_{0.48}Na_{0.52})(Nb_{0.95}Sb_{0.05})$–$0.04Bi_{0.5}(Na_{0.82}K_{0.18})_{0.5}ZrO_3$–*x*Sm lead-free ceramics. *J Adv Ceram* 2020, **9**: 72–82.
[53] ASTM. *Annual Book of ASTM Standards*. *Section 8*: *Plastics*. West Conshohocken, USA: ASTM International, 2004, **8**: D2383–D4322.
[54] Shekhawat P, Sharma G, Singh RM. Microstructural and morphological development of eggshell powder and flyash-based geopolymers. *Constr Build Mater* 2020, **260**: 119886.
[55] Petlitckaia S, Poulesquen A. Design of lightweight metakaolin based geopolymer foamed with hydrogen peroxide. *Ceram Int* 2019, **45**: 1322–1330.
[56] Bai CY, Colombo P. High-porosity geopolymer membrane supports by peroxide route with the addition of egg white as surfactant. *Ceram Int* 2017, **43**: 2267–2273.
[57] Bai CY, Franchin G, Elsayed H, *et al*. High strength metakaolin-based geopolymer foams with variable macroporous structure. *J Eur Ceram Soc* 2016, **36**: 4243–4249.
[58] Qiao YJ, Li XY, Bai CY, *et al*. Effects of surfactants/stabilizing agents on the microstructure and properties of porous geopolymers by direct foaming. *J Asian Ceram Soc* 2021, **9**: 412–423.
[59] Wu JD, Zhang ZR, Zhang Y, *et al*. Preparation and characterization of ultra-lightweight foamed geopolymer (UFG) based on fly ash–metakaolin blends. *Constr Build Mater* 2018, **168**: 771–779.
[60] Novais RM, Ascensão G, Tobaldi DM, *et al*. Biomass fly ash geopolymer monoliths for effective methylene blue removal from wastewaters. *J Clean Prod* 2018, **171**: 783–794.
[61] Novais RM, Ascensão G, Buruberri LH, *et al*. Influence of blowing agent on the fresh- and hardened-state properties of lightweight geopolymers. *Mater Design* 2016, **108**: 551–559.
[62] Novais RM, Buruberri LH, Ascensão G, *et al*. Porous biomass fly ash-based geopolymers with tailored thermal conductivity. *J Clean Prod* 2016, **119**: 99–107.
[63] Rice RW. Comparison of stress concentration versus minimum solid area based mechanical property–porosity relations. *J Mater Sci* 1993, **28**: 2187–2190.
[64] Strozi Cilla M, Raymundo Morelli M, Colombo P. Effect of process parameters on the physical properties of porous geopolymers obtained by gelcasting. *Ceram Int* 2014, **40**: 13585–13590.
[65] Franchin G, Pesonen J, Luukkonen T, *et al*. Removal of ammonium from wastewater with geopolymer sorbents fabricated via additive manufacturing. *Mater Design* 2020, **195**: 109006.
[66] Luhar I, Luhar S, Abdullah MMAB, *et al*. A state-of-the-art review on innovative geopolymer composites designed for water and wastewater treatment. *Materials* 2021, **14**: 7456.
[67] Jaimes JE, Montaño AM, González CP. Geopolymer derived from bentonite: Structural characterization and evaluation as a potential sorbent of ammonium in waters. *J Phys Conf Ser* 2020, **1587**: 012008.
[68] Luukkonen T, Sarkkinen M, Kemppainen K, *et al*. Metakaolin geopolymer characterization and application for ammonium removal from model solutions and landfill leachate. *Appl Clay Sci* 2016, **119**: 266–276.
[69] Tchakouté HK, Rüscher CH, Hinsch M, *et al*. Utilization of sodium waterglass from sugar cane bagasse ash as a new alternative hardener for producing metakaolin-based geopolymer cement. *Geochemistry* 2017, **77**: 257–266.
[70] Sanguanpak S, Wannagon A, Saengam C, *et al*. Porous metakaolin-based geopolymer granules for removal of ammonium in aqueous solution and anaerobically pretreated piggery wastewater. *J Clean Prod* 2021, **297**: 126643.
[71] Max JJ, Chapados C. Aqueous ammonia and ammonium

chloride hydrates: Principal infrared spectra. *J Mol Struct* 2013, **1046**: 124–135.
[72] Da Silva VJ, da Silva MF, Gonçalves WP, *et al*. Porous mullite blocks with compositions containing kaolin and alumina waste. *Ceram Int* 2016, **42**: 15471–15478.
[73] Lee WE, Souza GP, McConville CJ, *et al*. Mullite formation in clays and clay-derived vitreous ceramics. *J Eur Ceram Soc* 2008, **28**: 465–471.
[74] Nath S, Biswas K, Wang KS, *et al*. Sintering, phase stability, and properties of calcium phosphate–mullite composites. *J Am Ceram Soc* 2010, **93**: 1639–1649.
[75] Omerašević M, Kocjan A, Bučevac D. Novel cordierite–acicular mullite composite for diesel particulate filters. *Ceram Int* 2022, **48**: 2273–2280.
[76] Guo HS, Li WF, Ye FB. Low-cost porous mullite ceramic membrane supports fabricated from kyanite by casting and reaction sintering. *Ceram Int* 2016, **42**: 4819–4826.
[77] Li N, Zhang XY, Qu YN, *et al*. A simple and efficient way to prepare porous mullite matrix ceramics via directly sintering SiO_2–Al_2O_3 microspheres. *J Eur Ceram Soc* 2016, **36**: 2807–2812.
[78] Han Y, Zhou LJ, Liang YX, *et al*. Fabrication and properties of silica/mullite porous ceramic by foam-gelcasting process using silicon kerf waste as raw material. *Mater Chem Phys* 2020, **240**: 122248.
[79] Feng G, Jiang F, Jiang WH, *et al*. Novel facile nonaqueous precipitation *in-situ* synthesis of mullite whisker skeleton porous materials. *Ceram Int* 2018, **44**: 22904–22910.
[80] Aboul-Gheit AK. A study of heat-treated ammonium-ion-exchanged zeolites by differential scanning calorimetry. *Thermochim Acta* 1988, **129**: 301–307.
[81] Rahier H, Wastiels J, Biesemans M, *et al*. Reaction mechanism, kinetics and high temperature transformations of geopolymers. *J Mater Sci* 2007, **42**: 2982–2996.
[82] Rashad M, Balasubramanian M. Characteristics of porous mullite developed from clay and $AlF_3{\cdot}3H_2O$. *J Eur Ceram Soc* 2018, **38**: 3673–3680.
[83] Li SJ, Zhao XQ, Hou GL, *et al*. Thermomechanical properties and thermal cycle resistance of plasma-sprayed mullite coating and mullite/zirconia composite coatings. *Ceram Int* 2016, **42**: 17447–17455.
[84] Su CC, Zhang YH, Wang LC, *et al*. Mechanical properties of reinforced porcelain slabs with mullite whiskers introduced by aluminum silicate fiber. *Ceram Int* 2022, **48**: 18909–18917.
[85] Wang W, Weng D, Wu XD. Thermal behavior of zirconia-doped mullite gel fibers. *Prog Nat Sci Mater Int* 2012, **22**: 213–218.
[86] Yan KZ, Guo YX, Fang L, *et al*. Decomposition and phase transformation mechanism of kaolinite calcined with sodium carbonate. *Appl Clay Sci* 2017, **147**: 90–96.
[87] Kurajica S, Tkalcec E, Schmauch J. $CoAl_2O_4$–mullite composites prepared by sol–gel processes. *J Eur Ceram Soc* 2007, **27**: 951–958.
[88] Li TZ, Wang J, Ruan J, *et al*. Crystallization behavior of transparent Na_2O–Al_2O_3–SiO_2 glass-ceramic containing rare-earth oxides. *J Non Cryst Solids* 2021, **567**: 120935.
[89] Yan XH, Yuan L, Liu ZL, *et al*. Preparation of porous mullite ceramic for high temperature flue gas filtration application by gel casting method. *J Aust Ceram Soc* 2021, **57**: 1189–1198.
[90] Kucuk A, Clare AG, Jones LE. Differences between surface and bulk properties of glass melts I. Compositional differences and influence of volatilization on composition and other physical properties. *J Non Cryst Solids* 2000, **261**: 28–38.
[91] Tsuchiyama A, Nagahara H, Kushiro I. Volatilization of sodium from silicate melt spheres and its application to the formation of chondrules. *Geochim Cosmochim Ac* 1981, **45**: 1357–1367.
[92] McCarthy GJ. High-level waste ceramics: Materials considerations, process simulation, and product characterization. *Nucl Technol* 1977, **32**: 92–105.
[93] Bell AMT, Backhouse DJ, Deng W, *et al*. X-ray fluorescence analysis of feldspars and silicate glass: Effects of melting time on fused bead consistency and volatilisation. *Minerals* 2020, **10**: 442.
[94] Pike RD. Volatilization of phosphorous from phosphate rock. *Ind Eng Chem* 1930, **22**: 344–349.
[95] Dong GP, Wu BT, Zhang FT, *et al*. Broadband near-infrared luminescence and tunable optical amplification around 1.55 μm and 1.33 μm of PbS quantum dots in glasses. *J Alloys Compd* 2011, **509**: 9335–9339.
[96] Li ZY, Fu LP, Gu HZ, *et al*. Fabrication of *in-situ* Ti(C,N) phase toughened Al_2O_3 based ceramics from natural bauxite. *Ceram Int* 2021, **47**: 25497–25504.
[97] Luhar I, Luhar S. A comprehensive review on fly ash-based geopolymer. *J Compos Sci* 2022, **6**: 219.
[98] Gualtieri A, Bellotto M, Artioli G, *et al*. Kinetic study of the kaolinite–mullite reaction sequence. Part II: Mullite formation. *Phys Chem Miner* 1995, **22**: 215–222.
[99] Ren Q, Li HH, Wu XL, *et al*. Effect of the calcining temperatures of low-grade bauxite on the mechanical property of mullite ceramics. *Int J Appl Ceram Technol* 2018, **15**: 554–562.
[100] Kim KH, Kim DH, Ryu SC, *et al*. Porous mullite/alumina-layered composites with a graded porosity fabricated by camphene-based freeze casting. *J Compos Mater* 2020, **54**: 1527–1534.
[101] Ji ZY, Yuan JS, Li XG. Removal of ammonium from wastewater using calcium form clinoptilolite. *J Hazard Mater* 2007, **141**: 483–488.
[102] Yang K, Bryce K, Zhu WG, *et al*. Multicomponent pyrochlore solid solutions with uranium incorporation—A new perspective of materials design for nuclear applications. *J Eur Ceram Soc* 2021, **41**: 2870–2882.
[103] Abdullayev A, Zemke F, Gurlo A, *et al*. Low-temperature fluoride-assisted synthesis of mullite whiskers. *RSC Adv* 2020, **10**: 31180–31186.
[104] Wu LH, Li CW, Chen YF, *et al*. Seed assisted *in-situ*

synthesis of porous anorthite/mullite whisker ceramics by foam-freeze casting. *Ceram Int* 2021, **47**: 11193–11201.
[105] Ma XX, Tian YM, Zhou Y, *et al*. Sintering temperature dependence of low-cost, low-density ceramic proppant with high breakage resistance. *Mater Lett* 2016, **180**: 127–129.
[106] Igami Y, Ohi S, Miyake A. Sillimanite-mullite transformation observed in synchrotron X-ray diffraction experiments. *J Am Ceram Soc* 2017, **100**: 4928–4937.
[107] Liu ZY, Wu CM, Xie N, *et al*. Mechanical properties of *in situ* synthesized mullite-based composite ceramics with three-dimensional network structure. *Int J Appl Ceram Technol* 2022, **19**: 1659–1668.
[108] Wu DJ, Zhao DK, Huang YF, *et al*. Shaping quality, microstructure, and mechanical properties of melt-grown mullite ceramics by directed laser deposition. *J Alloys Compd* 2021, **871**: 159609.
[109] Yang ZC, Yang FY, Zhao S, *et al*. *In-situ* growth of mullite whiskers and their effect on the microstructure and properties of porous mullite ceramics with an open/closed pore structure. *J Eur Ceram Soc* 2021, **41**: 299–308.
[110] Yadav AK, Patel S, Bhattacharyya S. Preparation of low-cost porous mullite ceramics by recycling fly ash. *AIP Conf Proc* 2019, **2142**: 030004.
[111] Zhang RB, Ye CS, Hou XB, *et al*. Microstructure and properties of lightweight fibrous porous mullite ceramics prepared by vacuum squeeze moulding technique. *Ceram Int* 2016, **42**: 14843–14848.
[112] Liu DZ, Hu P, Zhao GD, *et al*. Silica bonded mullite fiber composite with isotropic geometry and properties for thermal insulating. *J Alloys Compd* 2017, **728**: 1049–1057.
[113] Wang X, Chen H, Zhao L, *et al*. Relation between rheological and curing behavior of inorganic foam slurries in the gel-casting process. *Ind Eng Chem Res* 2018, **57**: 4261–4267.
[114] Liu XY, Ge ST, Zhang HJ, *et al*. Foam-gelcasting preparation of $ZrSiO_4$ modified porous mullite ceramics. *Ceram-Silikáty* 2020: 365–370.
[115] Yuan L, Ma BY, Zhu Q, *et al*. Preparation and properties of mullite-bonded porous fibrous mullite ceramics by an epoxy resin gel-casting process. *Ceram Int* 2017, **43**: 5478–5483.
[116] Deng XG, Ji P, Yin JQ, *et al*. Fabrication and characterization of mullite-whisker-reinforced lightweight porous materials with $AlF_3{\cdot}3H_2O$. *Ceram Int* 2022, **48**: 14891–14898.
[117] Yang FK, Li CW, Lin YM, *et al*. Fabrication of porous mullite ceramics with high porosity using foam-gelcasting. *Key Eng Mater* 2012, **512–515**: 580–585.
[118] Yang FK, Li CW, Lin YM, *et al*. Effects of sintering temperature on properties of porous mullite/corundum ceramics. *Mater Lett* 2012, **73**: 36–39.
[119] Guo HS, Ye FB, Li WF, *et al*. Preparation and characterization of foamed microporous mullite ceramics based on kyanite. *Ceram Int* 2015, **41**: 14645–14651.
[120] Gong LL, Wang YH, Cheng XD, *et al*. Porous mullite ceramics with low thermal conductivity prepared by foaming and starch consolidation. *J Porous Mater* 2014, **21**: 15–21.
[121] Zhang RB, Hou XB, Ye CS, *et al*. Enhanced mechanical and thermal properties of anisotropic fibrous porous mullite–zirconia composites produced using sol–gel impregnation. *J Alloys Compd* 2017, **699**: 511–516.
[122] Gao S, Zhang YF, Zhang YM. Preparation of low-cost foam ceramics with mullite extracted from fly ash. *J Ceram Soc Jpn* 2020, **128**: 812–820.
[123] Zhou XZ, Zhu SF, Wang YX, *et al*. Preparation of porous mullite–corundum ceramics via organic foam impregnation. *Korean J Mater Res* 2022, **32**: 85–93.
[124] Gong LL, Wang YH, Cheng XD, *et al*. Thermal conductivity of highly porous mullite materials. *Int J Heat Mass Transf* 2013, **67**: 253–259.